RSC Advances

ROYAL SOCIETY OF CHEMISTRY

www.rsc.org/advances

Nitrogen-doped porous carbon foams prepared from mesophase pitch through graphitic carbon nitride nanosheet templates

Rui-Lun Xie,[a] Zhi-Min Zong,[*a] Fang-Jing Liu,[a] Yu-Gao Wang,[a] Hui-Long Yan,[a] Zhe-Hao Wei,[b] Mohannad Mayyas[a] and Xian-Long Wei[a]

[a] *Key Laboratory of Coal Processing and Efficient Utilization, Ministry of Education, China University of Mining & Technology, Xuzhou 221116, China.*

[b] *The Gene & Linda Voiland School of Chemical Engineering and Bioengineering, Washington State University, Pullman WA 99164, USA.*

ABSTRACT: A scalable and facile method was developed to synthesize nitrogen-doped porous carbon foams (NPCFs) using graphitic carbon nitride (g-C_3N_4) nanosheets as hard templates through the calcination of mesophase pitch. The morphology, structure, chemical composition and electrochemical performance of the as-prepared NPCFs were characterized and investigated. The results show that NPCFs are fabricated from the crimpled and folded carbon nanosheets and have a three-dimensional interconnected structure. The carbon nanosheets show a certain degree of orientation of graphite crystallites. The specific surface area, wall thickness and nitrogen content are controllable by tuning the mass ratio of g-C_3N_4 nanosheets to mesophase pitch. The nitrogen content, which mainly consists of quaternary-N and pyridinic-N components, significantly decreases from 6.48 to 0.74 at% with raising calcination temperature from 800 to 1600 ^{o}C. The NPCFs prepared at 800 ^{o}C have a high specific surface area of 2098 m^2 g^{-1}, an ultra-large pore volume of 5.048 cm^3 g^{-1} and a high nitrogen content of 6.48 at%. Furthermore, this material exhibits remarkable electrochemical performance as electrode material for supercapacitor with a specific capacitance of 125.6 F g^{-1} even at a high scan rate of 200 mV s^{-1}.

[*] Corresponding author. Tel: +86 516 83885951; fax: +86 516 83884399.
E-mail address: zong_zhimin@163.com (Z. M. Zong).

1. Introduction

Porous carbon foams (PCFs) have attracted much attention from both industry and academia in the areas of supercapacitors, lithium batteries and catalyst supports, due to their large specific surface areas, large specific porous volumes, high electronic conductivity and interconnected conductive networks.[1-4] To fully utilize these properties, PCFs are widely synthesized into heteroatom-doped porous carbon materials via the incorporation of large quantities of heteroatoms into the structure of PCFs. As an important element, nitrogen is deemed to be a promising candidate for improving the performance of PCFs, because it has comparable atomic size with carbon atom and can form the strong valence bonds with carbon atoms.[5] Therefore, nitrogen-doped porous carbon foams (NPCFs) with different structures have been successfully prepared. So far, NPCFs have been synthesized through two main approaches: one is post-treatment doping, including modification in aminocaproic acid,[6] heat treatment in ammonia,[7,8] arc-discharge in pyridine or ammonia vapor,[9] and ionic liquid treatment,[10] and another is direct synthesis from nitrogen-containing precursors,[11] such as chemical vapor deposition,[12,13] template method,[14,15] and direct pyrolysis[16, 17]. Among the techniques, the template method is most frequently used. Most recently, Yan *et al*. prepared NPCFs with different nitrogen contents using nano-$CaCO_3$ as hard template and polydopamine as carbon and nitrogen precursor.[18] Pan *et al*. fabricated the nitrogen-doped hierarchical porous carbon material by a two-step method using nano-SiO_2 as hard template.[19] The dominant roles of hard templates have been hitherto played by one-dimensional materials and three-dimensional (3D) materials. However, there were few reports on the synthesis of NPCFs using nanosheet materials as hard templates. Most fabrication methods of NPCFs using hard templates impose massive environmental and economic costs, especially for large-scale production. For example, preparation through silica nanoparticle template route remains a predominant synthesis method and a feasible

approach to low-cost industrialization, but limited by the harsh running conditions and the use of toxic reagents such as NaOH and HF.[20,21] To solve the problems mentioned above, developing a cheap and eco-friendly material as the hard template is of crucial importance.

In this investigation, a novel material of graphitic carbon nitride (g-C_3N_4), which can be prepared by cyanamide, dicyandiamide, melamine and urea, was used as the hard template to fabricate NPCFs.[22-24] Currently, g-C_3N_4 has been successfully employed as sacrificial template to synthesize a macroscopic graphene monolith with large specific surface area (SSA) and high nitrogen content through the calcination of glucose at high temperatures.[25] The as-prepared graphene monolith showed a superior electrocatalytic activity for oxygen reduction reaction when it was used as electrocatalyst. Moreover, the decomposition of g-C_3N_4 at high temperatures could introduce nitrogen atoms and/or nitrogen-containing groups into the structure of PCFs to prepare NPCFs.[22,26] Thus, g-C_3N_4 can be used as an excellent nitrogen source for preparing NPCFs in a green route. To our knowledge, few reports were issued on studying the synthesis of NPCFs by using this economic and eco-friendly technique.

Herein, large amounts of NPCFs in high yields were synthesized by a scalable and simple method via self-assembly of both mesophase pitch (MP) as the precursor and g-C_3N_4 nanosheets as hard templates. The morphology and microstructure of the resultant NPCFs were characterized and the influence of calcination temperature (CT) and mass ratio of g-C_3N_4 nanosheets to MP ($MR_{g/m}$) in the structural and textural characteristics of NPCFs was investigated. The electrochemical performance of the samples prepared at 800 ^{o}C as electrode material for supercapacitor was evaluated. The present study is aimed at the fabrication of NPCFs using new promising sacrificial templates of g-C_3N_4 nanosheets and this work will benefit the development of promising approaches for the synthesis of NPCFs.

2. Experimental

2.1. Materials

The MP was prepared in the laboratory and the urea was purchased from Sinopharm Chemical Reagent Co., Ltd., China. They were chopped into small pieces followed by desiccation in a vacuum oven at 80 °C for 24 h before use. All the organic solvents used in the experiments are analytical reagents and were purchased from Sinopharm Chemical Reagent Co., Ltd., China.

2.2. Preparation of NPCFs

In a typical preparation,[24] 10 g urea was first put into a crucible with a lid and then heated to 550 ^{o}C for 4 h with a heating rate of 4 ^{o}C min^{-1} in a tube furnace. After that, the yellow g-C_3N_4 powder was collected. Then, 0.4 g as-made g-C_3N_4 was dispersed into 200 mL tetrahydrofuran (THF) solution in a 250 mL spherical flask under vigorous agitation at room temperature for 3 h and subsequently sonicated for 6 h to obtain a mixture of suspended g-C_3N_4 nanosheets. Afterwards, the liquid/solid mixture was centrifuged at 500 rpm for 10 min to remove aggragates and obtain a homogeneous milk-like g-C_3N_4 nanosheet suspension with a concentration of *ca*. 2 mg mL^{-1}. Meanwhile, an appropriate amount of THF-soluble portion of MP was redissolved in THF. Both solutions of dissolved MP and g-C_3N_4 nanosheet suspension were thoroughly mixed together with different $MR_{g/m}$ under vigorous agitation at room temperature for 12 h followed by solvent evaporation at 70 ^{o}C in a water bath to obtain a pale yellow mixture. The mixture was set at 405 ^{o}C for 4 h to transform into grayish-black composites in a tube furnace under nitrogen atmosphere and subsequently calcined at different temperatures of 800, 1200 and 1600 ^{o}C for 2 h to remove g-C_3N_4 nanosheets. After the tube furnace was cooled down to room temperature, black materials were eventually obtained. The samples obtained at 800, 1200 and 1600 ^{o}C with $MR_{g/m}$ of 16 are denoted as NPCF-8, NPCF-12 and NPCF-16, respectively.

2.3. Characterizations

The morphology and microstructure of the samples were characterized using a Sirion200 scanning electron microscopy (SEM) operated at 30 kV and a Tecnai G2 F20 transition electron microscopy (TEM) operated at 200 kV. The thermal analysis was conducted using a SDTQ600 thermogravimetric analyzer (TGA) at a heating rate of 10 ^{o}C min^{-1}. X-ray diffraction (XRD) patterns were recorded on a Bruker D8 Advance diffractometer with Cu-Kα irradiation. The nitrogen adsorption/desorption analysis was carried out on an Autosorb-1-MP instrument at 77 K. The samples were also analyzed with a THERMO ESCALAB 250XI X-ray photoelectron spectroscopy (XPS) equipped with a monochromic Al-Kα source and a Lab RAM-HR Raman spectrometer using a 514.5 nm laser.

2.4. Electrochemical characterization

The electrochemical measurements of the individual electrode were carried out in a three-electrode system, in which the Pt foil, Ag/AgCl and Ni foam coated with as-prepared sample electrodes were used as the counter, reference and working electrodes, respectively. The working electrode was fabricated by pressing slurry mixtures of 80 wt% as-prepared sample, 7.5 wt% acetylene black, 7.5 wt% conducting graphite and 5 wt% polytetrafluoroethylene binder onto a nickel foam current collector and contained *ca*. 4.0 mg of active materials with an area of 1 cm^2. The cyclic voltammogram (CV), galvanostatic charge/discharge (GCD) and electrochemical impedance spectroscopy (EIS) measurements were performed in a 2 M NaOH electrolyte on a CHI 660C electrochemical workstation (Shanghai Chenhua Co., Ltd., China) at room temperature. The specific capacitance derived from CV curves was calculated according to the following equation: $C_m = \int I\mathrm{d}V/vmV$, where C_m, I, v, V and m represent the specific capacitance, response current, potential scan rate, potential and the mass of the prepared material in the electrode, respectively.

3. Results and discussion

Fig. 1 illustrates the synthesis approach of NPCFs involving the use of MP as precursor and g-C_3N_4 nanosheets with various thicknesses (see Figs. S1a and S1b in Supplementary Material) as sacrificial templates. Before calcination, the mixture of g-C_3N_4 nanosheets and MP was obtained as pale yellow bulks with a layered structure (Fig. S1c) due to the π-π interactions and hydrogen bonds. Then the mixture was turned into grayish-black composites (Fig. S1d) containing g-C_3N_4 nanosheets and aromatic carbon intermediates after calcination at 405 ^oC for more than 4 h. After heating the composites at temperatures higher than 800 ^oC, the g-C_3N_4 nanosheets underwent thermolysis and then the black NPCFs with a unique porous structure were achieved. The final yields of NPCFs are as high as 95 wt%, which is in accord with the results of TGA analysis (Fig. S2), showing the potential application for large-scale production.

XRD was employed to investigate the structural changes during calcination. As Fig. 2(a) displays, NPCF-8 shows a main diffraction peak at 25.4°, perhaps corresponding to the (002) crystal plane of turbostratic structure of NPCF-8,[27] while the characteristic diffraction peak of g-C_3N_4 appears at 27.4°, which is indexed as the (002) crystal plane of the g-C_3N_4.[28] The existence of only two diffraction peaks at 25.4° and 42.6° associated with carbon in the XRD pattern and the absence of the characteristic diffraction peaks of g-C_3N_4 suggest that the samples were obtained without any residual g-C_3N_4 nanosheets or other impurities. Meanwhile, according to the XRD analysis, the interlayer spacing (d_{002}) was calculated to be *ca*. 0.35 nm, which is slightly bigger than the value (0.34 nm) of ideal crystalline graphite. Thus, NPCFs containing graphite crystallites were prepared. Raman spectrometer was used to further investigate the crystallite structure of NPCFs obtained at different CTs and the disorder degree. As Fig. 2(b) displays, the typical Raman spectra exhibit three main peaks at 1347, 1580 and 2700 cm^{-1}, which are assigned to D, G and 2D bands, respectively.

The G band is attributed to the E_{2g} in-plane vibration from sp^2-bonded carbon domain, offering the information of graphitic carbon in the samples, whereas the D band originates from the A_{1g} in-plane breathing vibration, which is related to the structural disorder and defects.[29] Besides, the intensity ratio of D to G band commonly reflects the crystallinity of the prepared materials. As shown in Fig. 2(b), the G band around 1580 cm^{-1} in the Raman spectra is relatively strong and high, showing the presence of a certain amount of graphitized sheets, which is in good agreement with the results of XRD analysis. An obvious decrease in the intensity ratio of D to G band with raising CT indicates a typical increase in the number of sp^2 carbon atoms and a corresponding reduction of sp^3 carbon atoms. Furthermore, the 2D band around 2700 cm^{-1} in the Raman spectra becomes more sharper and higher with raising CT from 800 and 1200 to 1600 ^oC. These results suggest that NPCFs with a high graphitization degree could be achieved at high CTs.

The morphology and microstructure of NPCFs were characterized by SEM and TEM. As shown in Fig. 3a, the obtained samples are observed as monoliths with a layered and foam-like structure on a larger scale, which clearly reveals a continuous and interconnected 3D framework with pores in different sizes. Different from the PCFs with uniform pores synthesized using silica templates,[30,31] the samples possess a number of unordered nanoscale pores and abundant slit-like pores (Fig. 3b). These results indicate that g-C_3N_4 nanosheets are not only used as hard templates, but also play a significant role in generating the pores. As Figs. 3c and 3d show, the samples consist of significant numbers of graphene-like carbon nanosheets which randomly aggregate and entangle with each other. A notable structural feature of the graphene-like carbon nanosheets is the existence of the crimples along the surface of the entangled carbon nanosheets. Subsequently, the special morphology of ultrathin carbon nanosheets from NPCFs was further characterized by TEM image at increasing magnification shown in Fig. 4a, which displays the structure of partially overlapping carbon

nanosheets. As Fig. 4b exhibits, the carbon nanosheets with little overlapping show a well-defined edge, indicating that the wall thicknesses of carbon nanosheets are only several nanometers. In addition, as shown in high-resolution TEM image (inset in Fig. 4a), the graphite layers are stacked in an ordered manner on the local scale of the carbon nanosheets, showing a certain degree of orientation of graphite crystallites. However, the analyses with TEM, XRD and Raman spectrometer suggest that the carbon nanosheets of the samples are not completely graphitized due to the low temperature for graphitization. For further investigation on the morphological changes of the samples, wall thicknesses were tuned by varying the $MR_{g/m}$. The thicknesses decreased from dozens of nanometers to several nanometers with increasing $MR_{g/m}$ from 1 to 16, as can be estimated from the images in Fig. S3.

As shown in Fig. 5a, the adsorption/desorption isotherms for the samples obtained from the mixed precursor with different $MR_{g/m}$ show type IV isotherms and H_3 hysteresis loops, corresponding to the slit-like pores or sheet particles between carbon nanosheets in the samples.[22] The hysteresis loops of the samples obtained with $MR_{g/m}$ of 4, 8 and 16 occur at a low relative pressure of *ca*. 0.05, indicating that the samples are rich in longer slit-like microporosity. The corresponding pore size distributions ranging from 0.9 to 25 nm in Fig. 5b further confirm the dominant presence of abundant microporosities and mesoporosities in the samples. The pronounced pores of 0.9 nm in size could be analogous to the intergranular cavities in the carbon nanosheets and/or slit-like microporosities enclosed by carbon nanosheets, which could be related to the pieces of monolayer g-C_3N_4 sheets. By varying the $MR_{g/m}$ from 1, 4 and 8 to 16, the SSAs of the samples increase as displayed in Fig. 5c and Table S1 from 178.6, 866.7 and 1406 to 2098 m^2 g^{-1} respectively, implying that improving the $MR_{g/m}$ is beneficial to NPCFs with large SSAs and ultrathin walls, as shown in Fig. S3. Surprisingly, the SSA of NPCF-8 without any pretreatment is up to 2098 m^2 g^{-1}, which is

close to the theoretical value (2630 $m^2 g^{-1}$) of monolayer graphene sheet,[32] indicating the existence of large amounts of ultrathin carbon nanosheets. Furthermore, NPCF-8 has an ultra-large pore volume of 5.048 $cm^3 g^{-1}$, which is much higher than that of the ordered mesoporous carbons and the majority of the graphene-based materials reported.[33-35] Such combination of characteristics (ultra-large pore volume and high SSA) has not been observed in any other NPCFs.

Tian *et al*. reported that nitrogen atoms and/or groups could be inserted into the graphene lattice by the electrophilic substitution reaction between cyano fragments derived from the decomposition of g-C_3N_4 at high temperatures and activated carbons.[22] Based on this study, XPS analysis was performed to determine the chemical composition and the chemical bonding between carbon and nitrogen atoms in the prepared NPCF-8. A sharp and strong graphitic C1s peak, a moderate strong N1s peak and a weak O1s peak appear in Fig. 6a, indicating that the samples mainly consist of carbon and nitrogen with a small amount of oxygen. The high-resolution spectra in the C1s and N1s can be divided into different components. As Fig. 6b illustrates, the C1s spectra is deconvoluted into four distinct peaks because of the various bonding configurations of carbon atoms in the samples. In detail, the strong and asymmetric peak centered at 284.7 eV in the C1s spectra is typically assigned to the sp^2 carbon atoms, suggesting the presence of a large proportion of sp^2-hybridized carbon atoms.[36] The peaks centered at 285.7 and 287.2 eV in the C1s spectra are attributed to sp^2 carbon atoms and sp^3 carbon atoms bonded to nitrogen respectively, while the peak centered at 290.0 eV probably corresponds to sp^2-hybridized carbon atoms in the aromatic ring attached to the nitrogen.[26,37-39] The above results suggest that nitrogen was successfully introduced into the aromatic structure. As shown in Fig. 6c, there are four peaks with bonding energies of 398.4, 399.4, 401.1 and 402.6 eV in the deconvoluted N1s spectra, which are assigned to pyridinic-N (N-6), pyrrolic-N (N-5), quaternary-N (N-Q) and pyridine-N-oxide (N-X), respectively, [26,40] providing a

further convincing evidence on nitrogen doping into the aromatic structure. Among the nitrogen-containing species (NCSs), pyridinic-N (N-6) and quaternary-N (N-Q) are dominant, accounting for more than 70% of the total nitrogen content. Interestingly, the presence of pyridine-N-oxide (N-X) is probably due to the reaction of NCSs derived from the decomposition of g-C_3N_4 nanosheets with oxygen and/or water in the air during calcination. As Table 1 lists, the nitrogen contents in the samples are 6.48 at% at 800 ^oC, 3.06 at% at 1200 ^oC and only 0.74 at% at 1600 ^oC, suggesting that raising CT retarded nitrogen doping.

The electrochemical performance of as-prepared NPCF-8 as electrode material for supercapacitor was evaluated by CV, GCD and EIS measurements. As Fig. 7a reveals, the CV curves at scan rates from 10 mV s^{-1} to 200 mV s^{-1} show nearly rectangular shapes and a rapid current respond on voltage reversal at each end potential and the shapes of CV curves change little with the increase of scan rates even at 200 mV s^{-1}, which are the typical characteristic of electrical double-layer capacitance, indicating the superior electrochemical capacitive behavior. The maximum specific capacitance derived from CV curves was calculated to be *ca*. 135 F g^{-1} at 10 mV s^{-1}, which is higher or comparable to other recently reported values of some graphite nanosheet and graphene based materials, such as porous graphene nanoribbon (130 F g^{-1} at 1 mV s^{-1}),[41] hydrazine reduced graphene (95 F g^{-1} at A g^{-1}) and trigol reduced graphene (130 F g^{-1} at 1 A g^{-1}),[42] porous graphene film (130 F g^{-1} at 2 mV s^{-1}),[43] Nafion-functionalized reduced graphene oxide thin film (118.5 F g^{-1} at 1 A g^{-1}),[44] graphene nanosheet (65.5 F g^{-1} at 0.5 A g^{-1})[45], and defect-introduced graphene sheet (136 F g^{-1} at 500 mV s^{-1})[46]. Moreover, the specific capacitance at 200 mV s^{-1} was still up to 125.6 F g^{-1}, which is 93% of that at 10 mV s^{-1}, showing excellent capacitance retention at high scan rates. As Fig. 7b shows, all GCD curves at a variety of current densities of 0.5, 1, 2, 3 and 5 A g^{-1} display a symmetrical triangular shape and show a linear variation in the same potential

window in the range of -1 to 0 V, exhibiting a splendid electrochemical reversibility and high charging/discharging efficiency. EIS measurement was carried out to analyze the electron transfer and ion transport in the cell at a frequency range of 0.01 Hz to 100 kHz under an open circuit potential. As Fig. 7c exhibits, the EIS plot of NPCF-8 exhibits a straight line at the low-frequency region and a semicircle at the high-frequency region. The semicircle with a small radius at the high-frequency region is indicative of the lower charge transfer resistance and outstanding ionic conduction at the interfaces of electrolyte/electrode.[47] The following straight line at the low-frequency region represents the lower diffusive resistance of the ion diffusion and transport in the electrolyte. EIS data are fitted to an equivalent circuit which includes the Ohmic resistance R_s, the charge-transfer resistance R_{ct}, the double-layer capacitance Q_{dl} and the constant phase element Q_D using Z-view software, as shown in the inset in Fig. 7c. As Fig. 7d displays, the phase angle (-86°) at 0.01 Hz on the Bode phase plot is observed to be close to ideal value of -90°, suggesting the good capacitive behavior of the electrode material prepared. Based on the results above, it is reasonable to believe that NPCF-8 could be a promising candidate as electrode material for supercapacitors.

4. Conclusions

NPCFs were synthesized by self-assembly of MP as the carbon precursor and g-C_3N_4 nanosheets as hard templates. The g-C_3N_4 nanosheets play an important role in the preparation of NPCFs and the formation of microporosities and mesoporosities. The NPCFs show high SSAs, large pore volumes and high nitrogen contents and display an interconnected 3D framework with ultrathin carbon nanosheet walls. NPCF-8 has a high SSA of 2098 $m^2 g^{-1}$, an ultra-large pore volume of 5.048 $cm^3 g^{-1}$ and a high nitrogen content of 6.48 at% and exhibits a moderate electrochemical performance as electrode material for supercapacitor, suggesting that the new material may have promising

potential applications in energy storage devices. In addition, the simple and scalable method developed here may have possibilities of fabricating other two-dimensional nanomaterials into 3D macroscopic architectures.

Acknowledgements

This work was supported by the Fund from National Natural Science Foundation of China for Innovative Research Group (Grant 51221462), Strategic Chinese-Japanese Joint Research Program (Grant 2013DFG60060), the Research and Innovation Project for College Graduates of Jiangsu Province (Grant CXZZ13_0942), the Basic Research Program of Jiangsu Province (Grant BK20130171) and a Project Funded by the Priority Academic Program Development of Jiangsu Higher Education Institutions.

References

1 Y. Liang, F. Liang, H. Zhong, Z. Li, R. Fu and D. Wu, *J Mater Chem A*, 2013, **1**, 7000.

2 E. Kang, Y. S. Jung, A. S. Cavanagh, G. H. Kim, S. M. George, A. C. Dillon, J. K. Kim and J. Lee, *Adv Funct Mater*, 2011, **21**, 2430.

3 J. Klett, R. Hardy, E. Romine, C. Walls and T. Burchell, *Carbon*, 2000, **38**, 953.

4 F. Glenk, T. Knorr, M. Schirmer, S. Guetlein and B. J. M. Etzold, *Chem Eng Technol*, 2010, **33**, 698.

5 X. Li, X. Zhu, Y. Zhu, Z. Yuan, L. Si and Y. Qian, *Carbon*, 2014, **69**, 515.

6 V. A. Likholobov, L. G. P'Yanova, A. I. Boronin, S. V. Koshcheev, A. N. Salanov, O. N. Baklanova, O. A. Knyazheva and A. V. Veselovskaya, *Prot Met Phys Chem+*, 2011, **47**, 181.

7 B. Stöhr, H. Boehm and R. Schlögl, *Carbon*, 1991, **29**, 707.

8 F. Pan, Z. Cao, Q. Zhao, H. Liang and J. Zhang, *J Power Sources*, 2014, **272**, 8.

9 L. S. Panchokarla, K. S. Subrahmanyam, S. K. Saha, A. Govindaraj, H. R. Krishnamurthy, U.

278 V. Waghmare and C. N. R. Rao, *Adv Mater*, 2009, **21**, 4726.

279 10 G. Sethia and A. Sayari, *Energy Fuels*, 2014, **28**, 2727.

280 11 W. Shen and W. Fan, *J Mater Chem A*, 2013, **1**, 999.

281 12 Y. D. Xia and R. Mokaya, *Chem Mater*, 2005, **17**, 1553.

282 13 Z. Yang, Y. Xia, X. Sun and R. Mokaya, *J Phys Chem C*, 2006, **110**, 18424.

283 14 N. Liu, L. Yin, C. Wang, L. Zhang, N. Lun, D. Xiang, Y. Qi and R. Gao, *Carbon*, 2010, **48**,

284 3579.

285 15 M. Lezanska, P. Pietrzyk and Z. Sojka, *J Phys Chem C*, 2010, **114**, 1208.

286 16 B. Xu, H. Duan, M. Chu, G. Cao and Y. Yang, *J Mater Chem A*, 2013, **1**, 4565.

287 17 T. Takeichi, Y. Yamazaki, M. Zuo, A. Ito, A. Matsumoto and M. Inagaki, *Carbon*, 2001, **39**,

288 257.

289 18 L. Yan, X. Bo, Y. Zhang and L. Guo, *Electrochim Acta*, 2014, **137**, 693.

290 19 J. Zhou, Z. Zhang, W. Xing, J. Yu, G. Han, W. Si and S. Zhuo, *Electrochim Acta*, 2015, **153**, 68.

291 20 M. Zhou, F. Pu, Z. Wang and S. Y. Guan. *carbon* 2014, **68**, 185.

292 21 Y. D. Xia and R. Mokaya, *Adv Mater*, 2004, **16**, 1553.

293 22 L. L. Tian, X. Y. Wei, Q. C. Zhuang, C. H. Jiang, C. Wu, G. Y. Ma, X. Zhao, Z. M. Zong and S.

294 G. Sun, *Nanoscale*, 2014, **6**, 6075.

295 23 J. Zhang, M. Zhang, R. Q. Sun and X. Wang, *Angew Chem Int Ed*, 2012, **51**, 10145.

296 24 J. Liu, T. Zhang, Z. Wang, G. Dawson and W. Chen, *J Mater Chem*, 2011, **21**, 14398.

297 25 X. H. Li, S. Kurasch, U. Kaiser and M. Antonietti, *Angew Chem Int Ed*, 2012, **51**, 9689.

298 26 Z. H. Sheng, L. Shao, J. J. Chen, W. J. Bao, F. B. Wang and X. H. Xia, *Acs Nano*, 2011, **5**,

299 4350.

300 27 L. G. Florescu, E. Vasile, I. Sandu, I. Soare, C. Fleaca, R. Ianchis, C. Luculescu, E. Dutu, R.

Birjega, I. Morjan and I. Voicu, *Appl Surf Sci*, 2011, **257**, 5270.

28 X. Wang, X. Chen, A. Thomas, X. Fu and M. Antonietti, *Adv Mater*, 2009, **21**, 1609.

29 J. Yang, C. Tian, L. Wang and H. Fu, *J Mater Chem*, 2011, **21**, 3384.

30 R. Ryoo, S. H. Joo, M. Kruk and M. Jaroniec, *Adv Mater*, 2001, **13**, 677.

31 H. F. Yang, Y. Yan, Y. Liu, F. Q. Zhang, R. Y. Zhang, Y. Meng, M. Li, S. H. Xie, B. Tu and D. Y. Zhao, *J Phys Chem B*, 2004, **108**, 17320.

32 Y. Zhu, S. Murali, M. D. Stoller, K. J. Ganesh, W. Cai, P. J. Ferreira, A. Pirkle, R. M. Wallace, K. A. Cychosz, M. Thommes, D. Su, E. A. Stach and R. S. Ruoff, *Science*, 2011, **332**, 1537.

33 X. Fan, L. Zhang, G. Zhang, Z. Shu and J. Shi, *Carbon*, 2013, **61**, 423.

34 X. Y. Chen, C. Chen, Z. J. Zhang and D. H. Xie, *J Mater Chem A*, 2013, **1**, 10903.

35 Z. J. Zhang, C. Chen, P. Cui and X. Y. Chen, *J Power Sources*, 2013, **242**, 41.

36 H. Wang, C. Zhang, Z. Liu, L. Wang, P. Han, H. Xu, K. Zhang, S. Dong, J. Yao and G. Cui, *J Mater Chem*, 2011, **21**, 5430.

37 N. Liu, L. Yin, C. Wang, L. Zhang, N. Lun, D. Xiang, Y. Qi and R. Gao, *Carbon*, 2010, **48**, 3579.

38 A. Vinu, K. Ariga, T. Mori, T. Nakanishi, S. Hishita, D. Golberg and Y. Bando, *Adv Mater*, 2005, **17**, 1648.

39 C. Zhang, L. Fu, N. Liu, M. Liu, Y. Wang and Z. Liu, *Adv Mater*, 2011, **23**, 1020.

40 G. P. Hao, W. C. Li, D. Qian and A. H. Lu, *Adv Mater*, 2010, **22**, 853.

41 C. Zheng, X. Zhou, H. Cao, G. Wang and Z. Liu, *J Mater Chem A*, 2014, **2**, 7484.

42 D. Mhamane, S. M. Unni, A. Suryawanshi, O. Game, C. Rode, B. Hannoyer, S. Kurungot and S. Ogale, *J Mater Chem*, 2012, **22**, 11140.

43 W. H. Guo, T. J. Liu, P. Jiang and Z. J. Zhang, *J Colloid Interf Sci*, 2015, **437**, 304.

44 B. G. Choi, J. Hong, W. H. Hong, P. T. Hammond and H. Park, *ACS Nano*, 2011, **5**, 7205.

45 B. S. Shen, W. J. Feng, J. W. Lang, R. T. Wang, Z. X. Tai and X. B. Yan, *Acta Phys-Chim Sin* 2012, **28**, 1726.

46 W. Lee, S. Suzuki and M. Miyayama, *Electrochim Acta*, 2014, **142**, 240.

47 J. Luo, H. D. Jang and J. Huang, *ACS Nano*, 2013, **7**, 1464.

Figure captions

Fig. 1 Schematic illustration of the preparation of NPCFs.

Fig. 2 (a) XRD patterns of NPCF-8 and g-C_3N_4 nanosheets and (b) Raman spectra of NPCFs obtained at different CTs.

Fig. 3 (a-d) SEM images of NPCFs. White arrows in (b) image show observably slit-like pores.

Fig. 4 (a and b) TEM images of NPCFs. The inset of (a) image shows the high-resolution TEM image of carbon nanosheets.

Fig. 5 (a) Nitrogen adsorption and desorption isotherms, (b) pore size distributions and (c) SSAs of the samples obtained at 800 ^{o}C for 2 h with different $MR_{g/m}$ of 1, 4, 8 and 16.

Fig. 6 (a) General XPS spectra, (b) high-resolution C1s spectra and (c) high-resolution N1s spectra of NPGF-8.

Fig. 7 (a) CV curves at different scan rates, (b) GCD curves at different current densities, (c) EIS plots and (d) Bode phase plot of NPGF-8. The inset of (c) is the equivalent circuit of EIS.

Table caption

Table 1 Atomic ratio (%) of carbon, nitrogen and oxygen in the samples obtained at different CTs.

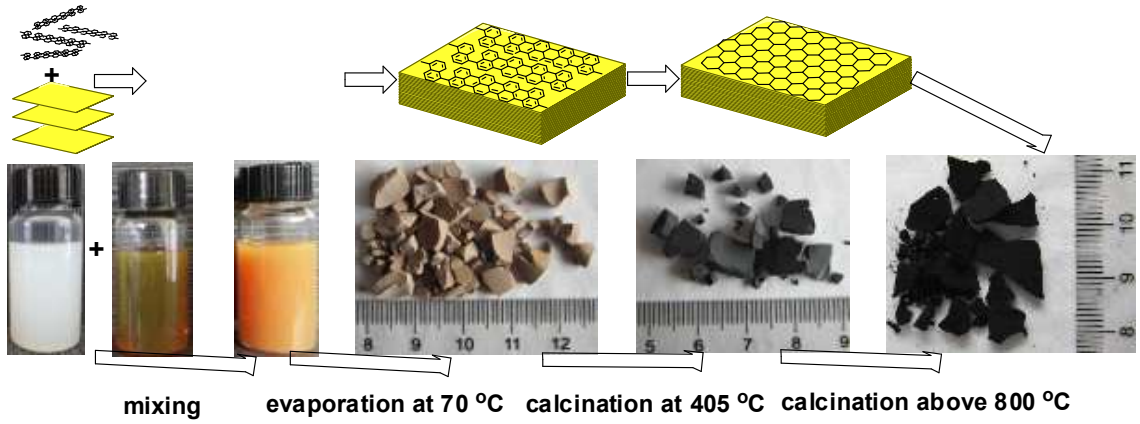

Fig. 1 Schematic illustration of the preparation of NPCFs.

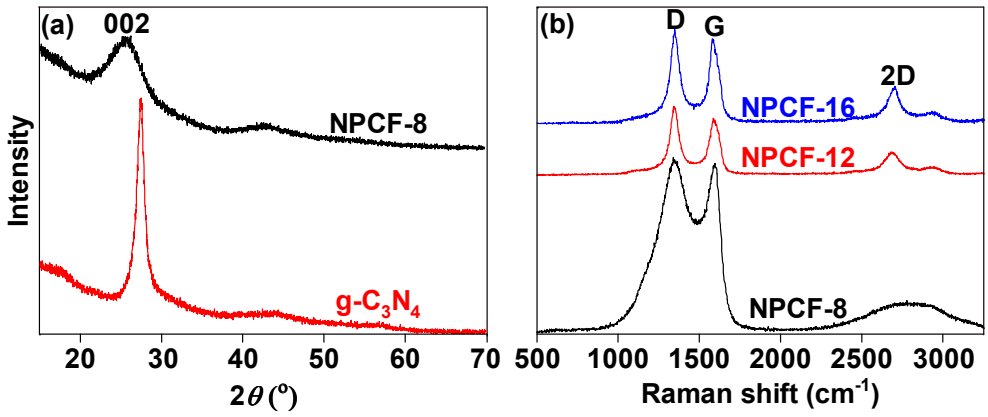

Fig. 2 (a) XRD patterns of NPCF-8 and g-C_3N_4 nanosheets and (b) Raman spectra of NPCFs obtained at different CTs.

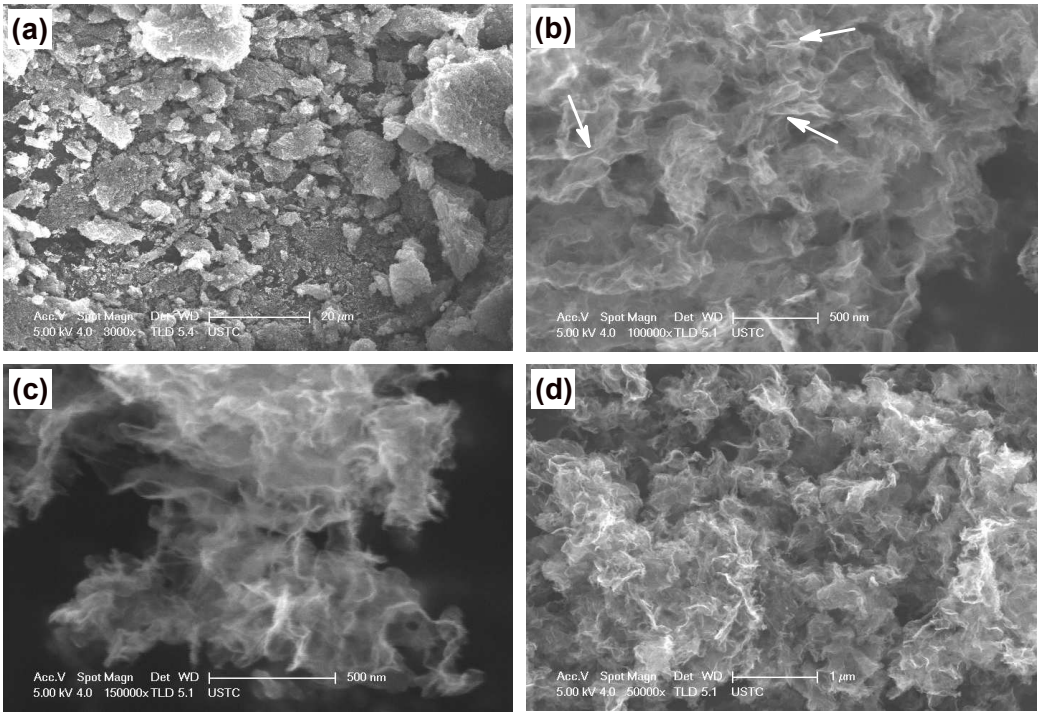

Fig. 3 (a-d) SEM images of NPCFs. White arrows in (b) image show observably slit-like pores.

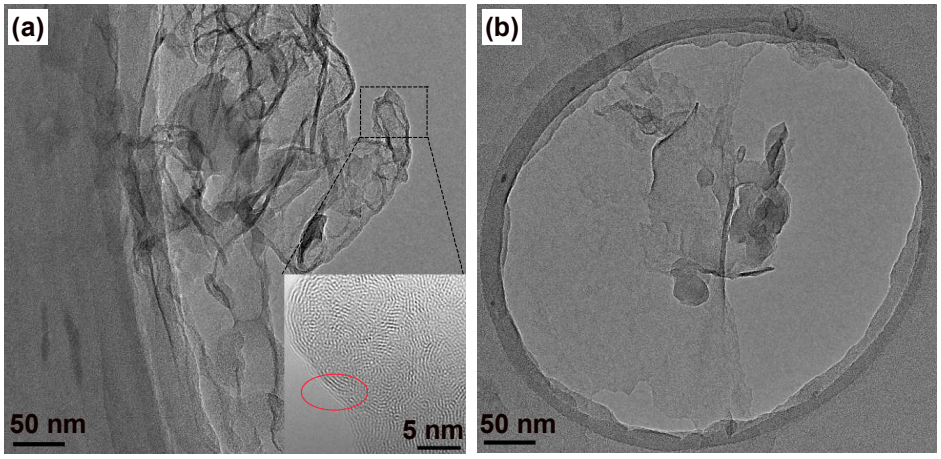

Fig. 4 (a and b) TEM images of NPCFs. The inset of (a) image shows the high-resolution TEM image of carbon nanosheets.

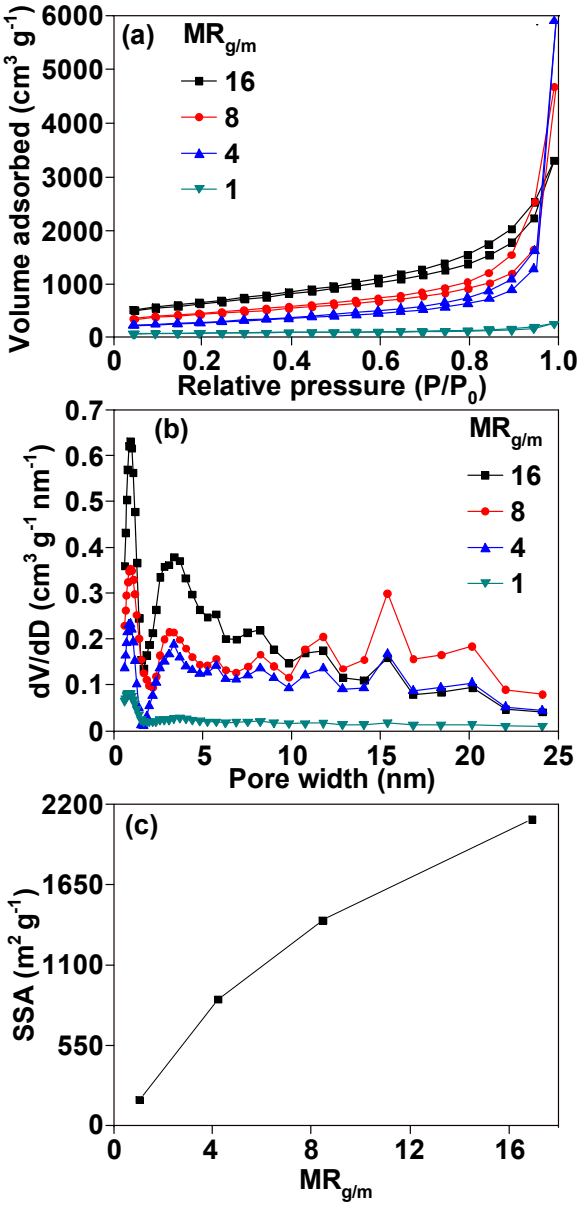

Fig. 5 (a) Nitrogen adsorption and desorption isotherms, (b) pore size distributions and (c) SSAs of the samples obtained at 800 ^{o}C for 2 h with different $MR_{g/m}$ of 1, 4, 8 and 16.

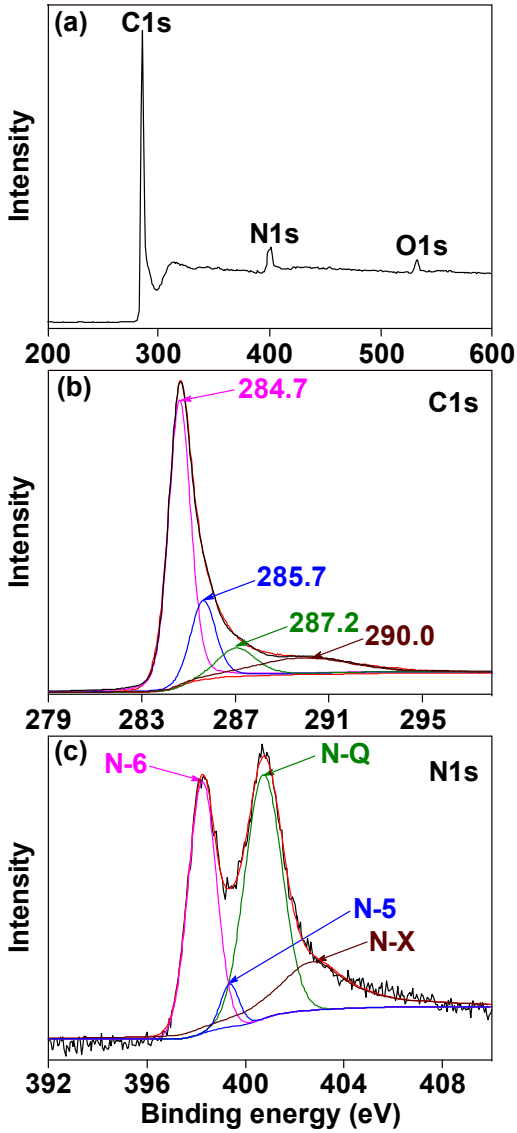

Fig. 6 (a) General XPS spectra, (b) high-resolution C1s spectra and (c) high-resolution N1s spectra of NPGF-8.

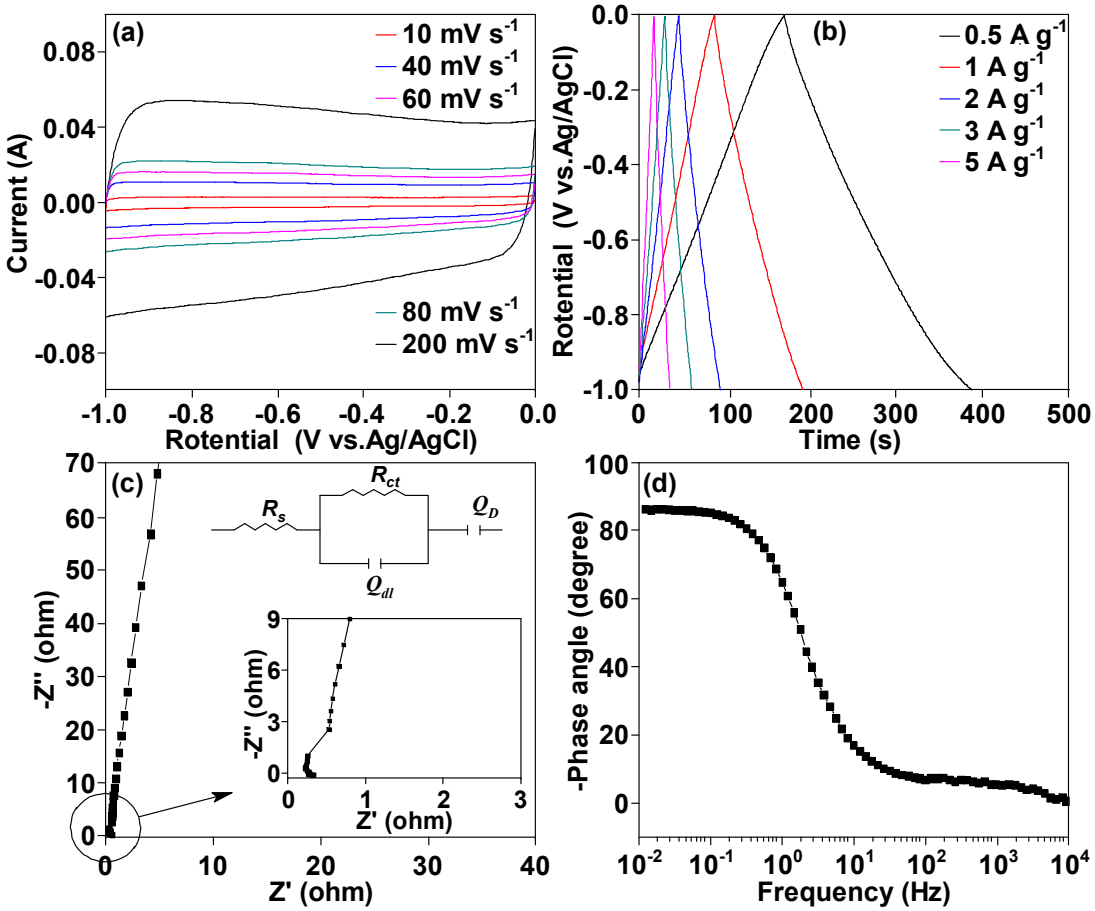

Fig. 7 (a) CV curves at different scan rates, (b) GCD curves at different current densities, (c) EIS plots and (d) Bode phase plot of NPGF-8. The inset of (c) is the equivalent circuit of EIS.

Table 1 Atomic ratio (%) of carbon, nitrogen and oxygen in the samples obtained at different CTs.

Sample	C1s	N1s	O1s
NPGF-8	90.61	6.48	2.91
NPGF-12	94.06	3.06	2.88
NPGF-16	96.44	0.74	2.82